Top-of-Atmosphere Direct Radiative Effect of Aerosols over the Tropical Oceans from the Clouds and the Earth's Radiant Energy System (CERES) Satellite Instrument

NORMAN G. LOEB AND SEIJI KATO

Center for Atmospheric Sciences, Hampton University, Hampton, Virginia

(Manuscript received 17 July 2001, in final form 7 December 2001)

ABSTRACT

Nine months of the Clouds and the Earth's Radiant Energy System (CERES)/Tropical Rainfall Measuring Mission (TRMM) broadband fluxes combined with the TRMM visible infrared scanner (VIRS) high-resolution imager measurements are used to estimate the daily average direct radiative effect of aerosols for clear-sky conditions over the tropical oceans. On average, aerosols have a cooling effect over the Tropics of 4.6 ± 1 W m^{-2}. The magnitude is ≈2 W m^{-2} smaller over the southern tropical oceans than it is over northern tropical oceans. The direct effect derived from CERES is highly correlated with coincident aerosol optical depth (τ) retrievals inferred from 0.63-μm VIRS radiances (correlation coefficient of 0.96). The slope of the regression line is ≈−32 W m^{-2} τ^{-1} over the equatorial Pacific Ocean, but changes both regionally and seasonally, depending on the aerosol characteristics. Near sources of biomass burning and desert dust, the aerosol direct effect reaches −25 to −30 W m^{-2}. The direct effect from CERES also shows a dependence on wind speed. The reason for this dependence is unclear—it may be due to increased aerosol (e.g., sea-salt or aerosol transport) or increased surface reflection (e.g., due to whitecaps). The uncertainty in the tropical average direct effect from CERES is ≈1 W m^{-2} (≈20%) due mainly to cloud contamination, the radiance-to-flux conversion, and instrument calibration. By comparison, uncertainties in the direct effect from the Earth Radiation Budget Experiment (ERBE) and CERES ''ERBE-like'' products are a factor of 3–5 times larger.

1. Introduction

Recent studies have demonstrated the potential influence of aerosols on top-of-atmosphere (TOA) and surface radiation budgets (Kiehl et al. 2000; Haywood and Boucher 2000). Aerosols affect the radiation budget directly by scattering and absorbing solar and thermal infrared radiation (Haywood et al. 1999; Satheesh et al. 1999), and indirectly by modifying the microphysical and radiative properties of clouds (Twomey 1974; Coakley et al. 1987; Albrecht 1989; Kaufman and Fraser 1997; Ackerman et al. 2000). The present study focuses on the TOA direct radiative effect of aerosols over ocean derived from the Clouds and the Earth's Radiant Energy System (CERES) instrument on board the Tropical Rainfall Measuring Mission (TRMM) spacecraft.

The direct radiative effect of aerosols at the TOA has previously been studied by combining satellite and in situ measurements over specific regions (Bergstrom and Russell 1999; Satheesh et al. 1999), from aircraft (Hignett et al. 1999), and by using satellite retrievals (King et al. 1999) as input to a radiative transfer model that computes TOA fluxes (e.g., Boucher and Tanré 2000). Only a handful of studies have actually used broadband satellite measurements to study the direct radiative effect of aerosols. Minnis et al. (1993) used broadband Earth Radiation Budget Experiment (ERBE) measurements (Barkstrom 1984) to estimate the radiative forcing by volcanic aerosols following the eruption of Mount Pinatubo. Christopher et al. (1996) used ERBE to estimate the instantaneous forcing by smoke aerosols over South America. Haywood et al. (1999) compared general circulation model (GCM) estimates of the direct effect with that inferred from ERBE. Satheesh et al. (1999) compared more recent TOA flux estimates from the CERES ''ERBE-like'' product with model calculations initialized using detailed in situ aerosol measurements over the Kaashidhoo Climate Observatory during the Indian Ocean Experiment (INDOEX). Christopher et al. (2000) and Li et al. (2000) used CERES and TRMM visible infrared scanner (VIRS) measurements to estimate direct radiative forcing from biomass burning aerosols over Central America.

Broadband measurements, such as from the ERBE (Barkstrom 1984) and the CERES instruments (Wielicki et al. 1996), eliminate the need for simplified model or empirical techniques that convert spectral fluxes from one or more imager channels to a broadband flux. In addition, since broadband instruments generally have onboard calibration sources, they tend to have better calibration accuracy and stability (Priestley et al. 2000)

Corresponding author address: Dr. Norman G. Loeb, NASA Langley Research Center, Mail Stop 420, Hampton, VA 23681-0001.
E-mail: n.g.loeb@larc.nasa.gov

than imagers. Many imagers used to study aerosols have no onboard calibration at visible wavelengths [e.g., Advanced Very High Resolution Radiometer (AVHRR); Polarization and Directionality of the Earth's Reflectances (POLDER)]. Consequently, broadband fluxes deduced from techniques that use multiple-channel imager radiances can suffer from larger calibration errors (Mischchenko et al. 1999). The main limitation of current broadband satellite measurements is their coarse spatial resolution; ERBE had a footprint size of ≈40 km (equivalent diameter), and CERES/TRMM had a resolution of ≈10 km at nadir. The lower spatial resolution makes it difficult to screen subfootprint-scale clouds from the analysis. Another major limitation involves the conversion of satellite radiances to fluxes. This is a source of uncertainty for all radiance-based approaches.

In this study, the impact of both of these limitations is reduced by using the more advanced CERES Single Satellite Footprint (SSF) product. The CERES SSF merges temporally and spatially collocated VIRS radiance measurements over each CERES footprint to identify cloud-free CERES fields of view. We demonstrate the improved effect of this change by comparing the direct effect based on scene identification from the CERES SSF with that deduced from the CERES ERBE-like product, which uses algorithms developed for ERBE but applied to CERES. Uncertainties in the radiance-to-flux conversion are reduced by a new set of angular models from multiangle CERES radiance measurements.

While it would be desirable to separate the anthropogenic effect of aerosols from their total effect, this remains highly uncertain from satellite measurements alone. Boucher and Tanré (2000) showed that estimates of the anthropogenic effect based on simple threshold techniques (e.g., using aerosol optical depth and the Ångström coefficient) were strongly dependent on the choice of the thresholds. As a result, the present analysis focuses only on the ''total'' effect of aerosols at the TOA.

2. Observations

The TRMM satellite was launched on 27 November 1997. The CERES instrument on board suffered a voltage converter anomaly in August 1998, and was turned off after 8 months of science data collection in September 1998. CERES/TRMM was turned back on in March 2000 in order to acquire data overlapping with the two CERES instruments aboard the *Terra* spacecraft, launched 18 December 1999. Unfortunately, the CERES/TRMM instrument acquired only one more month of science data before the voltage converter anomaly caused irreparable damage to electronic components downstream of the converter. In this study, all nine months of CERES/TRMM measurements are considered. We use the CERES/TRMM SSF TOA/Surface Fluxes and Clouds product from January to August 1998, and from March 2000, between 35°S and 35°N. The CERES SSF product combines CERES measurements of reflected shortwave (SW), emitted longwave (LW) and emitted window (WN) radiances and fluxes with coincident VIRS retrievals of aerosol and cloud properties. VIRS aerosol and cloud properties are convolved over the CERES footprint with the CERES point spread function. Also included in this product are meteorological fields based on the European Centre for Medium-Range Weather Forecasts (ECMWF) data assimilation analysis (Rabier et al. 1998). The CERES instrument has a resolution at nadir of approximately 10 km (equivalent diameter) and operates in three scan modes: cross-track, along-track, and rotating azimuth plane (RAP) mode, where the instrument scans in elevation as it rotates in azimuth. The VIRS instrument is a five-channel imaging spectroradiometer that measures radiation at 0.63, 1.61, 3.78, 10.8, and 12.0 μm. VIRS is similar to the AVHRR instrument but has a 2.11-km resolution at nadir compared to 1.1 km for AVHRR.

3. Methodology

The top-of-atmosphere direct radiative effect of aerosols for a given location at latitude λ and longitude ψ on a given day (d) is defined as follows:

$$\Delta F(\lambda, \psi, d) = \overline{F}_{na}(\lambda, \psi, d) - \overline{F}_{a}(\lambda, \psi, d), \quad (1)$$

where $\overline{F}_{na}(\lambda, \psi, d)$ is the daily average SW flux in the absence of aerosols, and $\overline{F}_{a}(\lambda, \psi, d)$ is the daily average SW flux in the presence of aerosols. The $\Delta F(\lambda, \psi, d)$ is determined from instantaneous CERES TOA fluxes that are converted to daily averages over $1° \times 1°$ regions. To avoid problems with specular reflection from the ocean surface, the analysis is restricted to solar zenith angles less than 60°, viewing zenith angles less than 70°, and glint angles (angle between reflected ray and specular ray for a flat ocean) greater than 40°.

a. Daily average flux with aerosols [$\overline{F}_{a}(\lambda, \psi, d)$]

Instantaneous fluxes are estimated from CERES broadband unfiltered radiances (Loeb et al. 2001) by dividing the radiances with anisotropic factors that account for the angular dependence of the radiance over the cloud-free ocean scene. These anisotropic factors are predetermined empirical angular distribution models (ADMs) that were constructed from nine months of CERES/TRMM cloud-free ocean observations. Separate clear-ocean ADMs were defined for four intervals of wind speed corresponding to the 0–25th, 25th–50th, 50th–75th, and 75th–100th percentiles of the wind speed probability density function. These correspond to wind speed intervals of approximately <3.5, 3.5–5.5, 5.5–7.5, and >7.5 m s^{-1}. For a given wind speed interval, w_k, the ADM is defined as follows:

$$R(w_k, \theta_o, \theta, \phi) = \frac{\pi \overline{I}(w_k, \theta_o, \theta, \phi)}{F(w_k, \theta_o)}, \quad (2)$$

where $\bar{I}(w_k, \theta_o, \theta, \phi)$ is the 9-month mean radiance for a given interval of solar zenith angle θ_o, viewing zenith angle θ, and relative azimuth angle ϕ; $F(w_k, \theta_o)$ is the corresponding flux determined by integration of $\bar{I}(w_k, \theta_o, \theta, \phi)$ over all upwelling directions. The wind speeds, which correspond to the 10-m level, are based on Special Sensor Microwave Imager (SSM/I) retrievals that have been ingested into the ECMWF data assimilation analysis. Instantaneous fluxes are determined as follows:

$$\hat{F} = \frac{\pi I(\theta_o, \theta, \phi)}{R(w_k, \theta_o, \theta, \phi)\left[\frac{R^{\text{th}}(w_k, I)}{R^{\text{th}}(w_k, \bar{I})}\right]}, \quad (3)$$

where $R^{\text{th}}(w_k, I)$ and $R^{\text{th}}(w_k, \bar{I})$ are theoretically derived anisotropic factors inferred from the measured CERES radiance $I(w_k, \theta_o, \theta, \phi)$ and the mean radiance $\bar{I}(w_k, \theta_o, \theta, \phi)$ used to derive $R(w_k, \theta_o, \theta, \phi)$. The ratio of theoretical anisotropic factors in Eq. (3) is introduced in order to account for the influence of aerosol optical depth on the anisotropy of the scene. Aerosol properties in the model calculations are based on the maritime tropical model of Hess et al. (1998). To ensure that this correction does not introduce a bias in the overall mean flux, fluxes estimated from Eq. (3) are normalized so that the mean estimated flux in each wind speed interval matches the flux $F(w_k, \theta_o)$ determined by integrating $\bar{I}(w_k, \theta_o, \theta, \phi)$ over all upwelling directions.

Each instantaneous flux is converted to a daily average by estimating what the corresponding flux would be under the same conditions at all other times of the day. To estimate the flux at any given time, directional models (Young et al. 1998) of normalized TOA albedo as a function of solar zenith angle are applied. The directional models are derived from the empirical ADMs described above. Each day, daily average fluxes $\bar{F}_a(\lambda, \psi, d)$ are sorted into 1° latitude × 1° longitude regions. While the assumption that aerosol conditions remain constant throughout the day may be inappropriate for episodic aerosols such as biomass burning and dust outbreaks, it is a reasonable assumption in average aerosol conditions, since diurnal variations are small (Holben et al. 2001).

b. Daily average flux with no aerosols [$\bar{F}_{na}(\lambda, \psi, d)$]

Since aerosols are always present in the atmosphere, $\bar{F}_{na}(\lambda, \psi, d)$ cannot be measured directly from satellite measurements. Instead, $\bar{F}_{na}(\lambda, \psi, d)$ is inferred by a simple regression procedure. Instantaneous TOA fluxes from CERES are plotted against VIRS 0.63-μm aerosol optical depths in 1° solar zenith angle increments. VIRS 0.63-μm aerosol optical depths are retrieved using the second-generation National Oceanic and Atmospheric Administration (NOAA)/National Environmental Satellite, Data, and Information Service (NESDIS) algorithm (Stowe et al. 1997), which has been implemented in the CERES SSF production code. The intercept for these regressions—that is, the TOA flux extrapolated to zero aerosol optical depth—approximates the "no aerosol flux" [$F_{na}(\theta_o)$] in each 1° solar zenith angle increment. Figure 1 shows the albedo corresponding to $F_{na}(\theta_o)$ against solar zenith angle. Also shown is a fifth-order polynomial fit (thick solid line) to this curve, and discrete ordinate (DISORT) radiative transfer model (Stamnes et al. 2000) calculations that account only for molecular scattering and absorption using *k*-distribution tables from Kato et al. (1999, thin lines). The calculations assume a tropical atmosphere with ocean surface bidirectional reflectance based on a routine ("OCEABRDF") from the 6S radiative transfer code (Vermote et al. 1997), which accounts for specular reflection (Cox and Munk 1955), wind speed dependent whitecaps (Koepke 1984), and below-water surface reflectance (Morel 1988). Here, wind speeds of 2, 5, and 10 m s^{-1} are assumed. The model results in Fig. 1 are within 3% (or ≈2 W m^{-2}) of $F_{na}(\theta_o)$ at solar zenith angles between 10° and 60°, and 5% elsewhere. Similar results are obtained when a midlatitude summer atmosphere is considered. This excellent agreement between theory and observation suggests that the model surface optics are well characterized in the calculations. The $\bar{F}_{na}(\lambda, \phi, d)$ for a given region is determined by averaging fluxes evaluated using the polynomial fit in Fig. 1 at all times of the day.

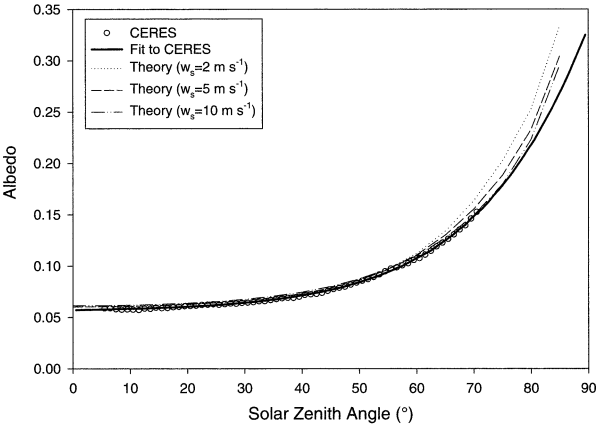

FIG. 1. Albedo against solar zenith angle for the "no aerosol" atmospheric condition inferred from CERES (open circles) and theory at three different wind speeds. The thick line is a fifth-order polynomial fit to the CERES result.

c. Clear-ocean scene identification

To identify clear-ocean scenes, a cloud mask (Trepte et al. 1999; Minnis et al. 1999) is applied to the VIRS pixel data. Briefly, the CERES cloud mask uses data from five VIRS channels to determine whether individual pixels contain cloud, glint, smoke, or fire signatures. The algorithm also ingests several parameters including clear-sky brightness temperature, reflectance, and their

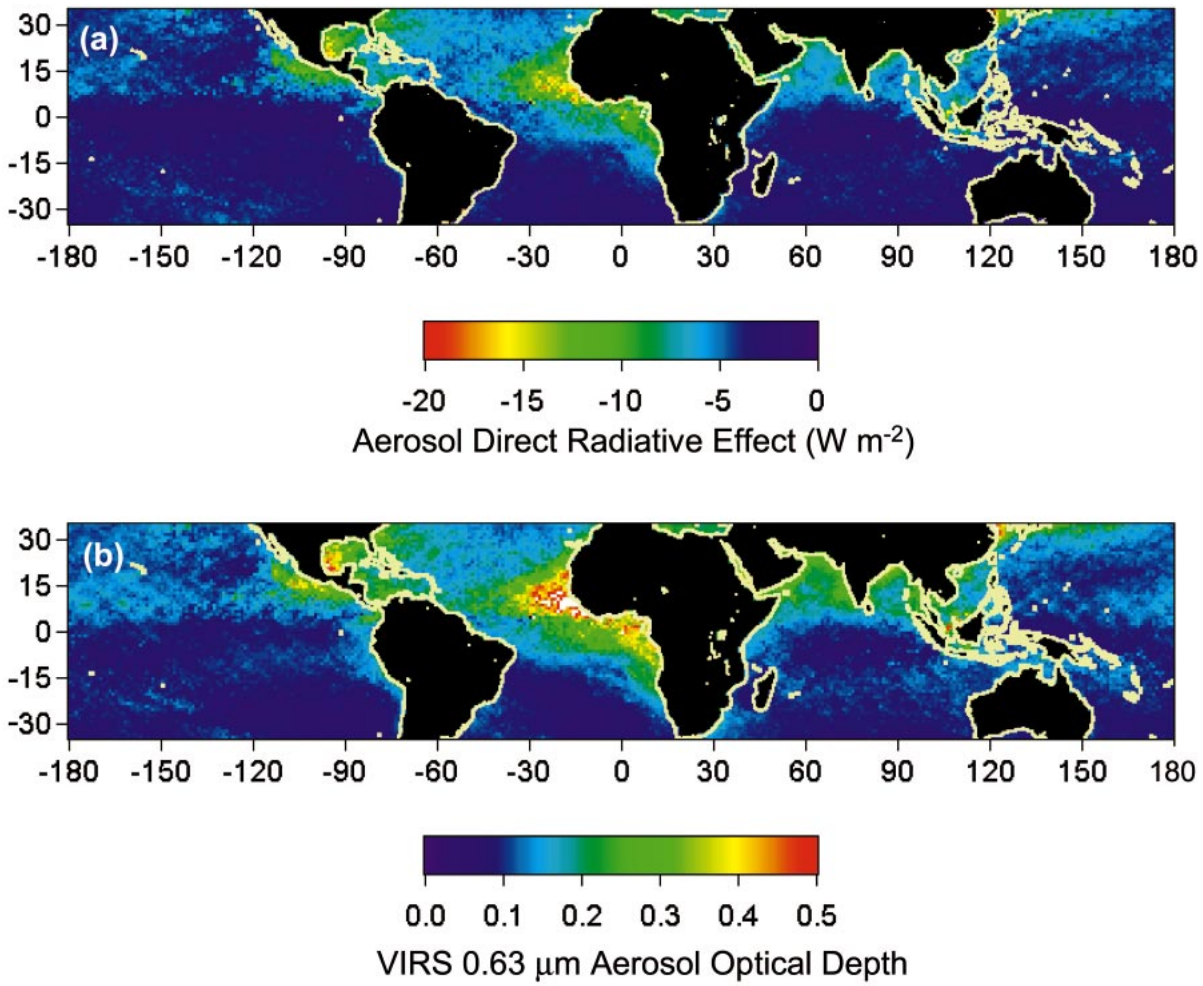

FIG. 2. (a) Direct radiative effect of aerosols and (b) mean VIRS 0.63-μm aerosol optical depth from nine months of CERES and VIRS observations.

standard deviation. The algorithm involves a three-step analysis of each pixel. The first step is a simple IR test that flags the pixels that are so cold they must be a cloud. Over ocean, this condition occurs if the VIRS 10.8-μm channel brightness temperature is more than 10°C below the ocean surface skin temperature. The second step involves a series of three tests comparing the pixel to a known background or clear-sky value for reflectance, brightness temperature, and infrared/near-infrared difference. The threshold values for these tests are determined from several sources, including empirically derived clear-sky albedo maps, surface skin temperature from numerical weather analyses, atmospheric temperature and humidity profiles (also from numerical weather analyses), and empirical spectral surface emissivity maps (Trepte et al. 1999). If all three tests unanimously determine the pixel to be clear, this pixel is labeled ''strong'' clear. If one or two tests fail, a series of relaxed tests are applied to determine whether or not the pixel can be labeled as ''weak'' clear.

Two additional threshold tests are also considered. The first is a spatial homogeneity test applied to VIRS pixels: if the maximum and minimum 0.63-μm reflectance from a 2×2 VIRS pixel array differs by more than a threshold value of 0.003, the pixels are considered potentially cloud contaminated. A second test identifies pixels with a 3.78-μm channel reflectance >0.03 as also potentially cloud contaminated. Thresholds for these tests are selected based on the analysis of Stowe et al. (1999).

If all VIRS pixels within a CERES footprint pass the reflectance, brightness temperature, and infrared/near-infrared difference tests, and more than 50% pass the spatial homogeneity and 3.78-μm channel reflectance tests, these footprints are considered clear and are included in the analysis. Section 5 examines uncertainties in the aerosol direct radiative effect due to cloud contamination.

4. Results

Figure 2a shows the direct radiative effect of aerosols based on Eq. (1) for all nine months of CERES/TRMM

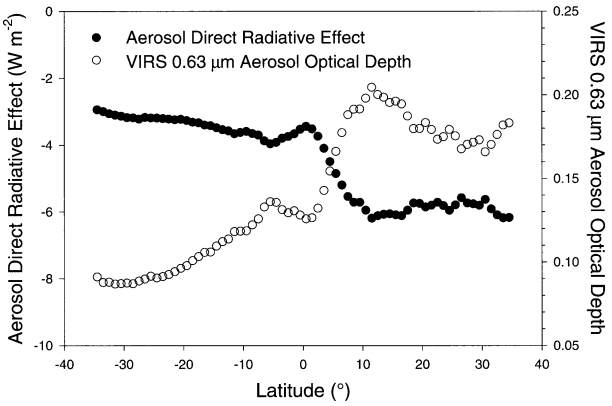

FIG. 3. Latitudinal distribution of the direct radiative effect of aerosols and VIRS 0.63-μm aerosol optical depth.

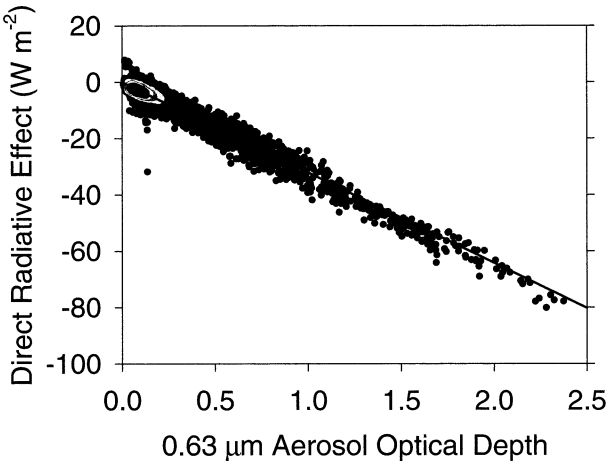

FIG. 4. The 1° regional daily mean direct radiative effect of aerosols against VIRS 0.63-μm aerosol optical depth for 10°S–20°N and 180°–90°W. Solid line is a linear regression fit through all data points.

observations. The mean VIRS 0.63-μm aerosol optical depth for the same period is shown in Fig. 2b. Areas of maximum aerosol direct radiative effect are clearly evident near Central America due to biomass burning, and west of the Sahara Desert associated with windblown, dust. In these regions, the 9-month mean aerosol direct effect can be greater than -20 W m^{-2} with VIRS 0.63-μm aerosol optical depths as high as 1.0. Minima in the 9-month mean aerosol direct radiative effect appear along the equatorial Pacific and Indian Oceans where easterly trade winds are <5 m s^{-1} (not shown). The direct radiative effect in these regions is typically -2 W m^{-2} and VIRS 0.63-μm aerosol optical depths range from 0.05 to 0.1. Latitudinal distributions of the direct radiative effect of aerosols and VIRS 0.63-μm aerosol optical depth are shown in Fig. 3. In both cases, a marked contrast between the northern and southern tropical oceans is evident. The direct radiative effect in the south is -3.6 compared to -5.5 W m^{-2} in the north. The corresponding VIRS 0.63-μm aerosol optical depths are 0.11 and 0.17, respectively. Over all the Tropics, the average direct radiative effect is -4.6 W m^{-2} and the average VIRS 0.63-μm aerosol optical depth is 0.14.

Figure 4 shows the relationship between the daily mean CERES direct radiative effect of aerosols and VIRS 0.63-μm average aerosol optical depth for 1° regions over the Pacific Ocean between 10°S–20°N and 180°–90°W. The two are highly correlated (correlation coefficient 0.96) and clearly show the influence of aerosols on TOA radiation, with values as high as -80 W m^{-2} (VIRS 0.63-μm aerosol optical depth of 2.5). As the aerosol optical depth approaches zero, the direct effect should also approach zero—in Fig. 4 it reaches 0.06 W m^{-2}, which is $\approx$1.3% (relative) of the tropical average aerosol direct radiative effect. The slope of the linear fit through the points—or the radiative effect of tropical aerosols per unit optical depth—is -32.1 W m^{-2} τ^{-1}. In contrast, Satheesh and Ramanathan (2000) obtained a value of -25 W m^{-2} τ^{-1} during the INDOEX campaign in a highly polluted period. The reason for the difference is likely due to increased aerosol absorption in the polluted air during INDOEX. To illustrate, Fig. 5a shows the solar zenith angle dependence in the derivative of aerosol direct radiative effect (in terms of albedo α) with VIRS 0.63-μm aerosol optical depth

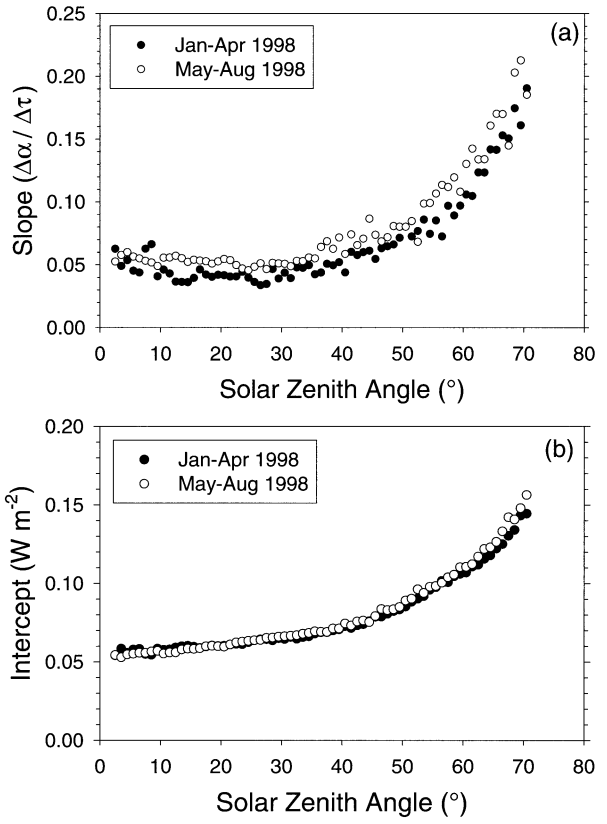

FIG. 5. (a) Slope and (b) intercept of CERES albedo against VIRS aerosol optical depth as function of solar zenith angle over KCO between Jan–Apr 1998 and May–Aug 1998.

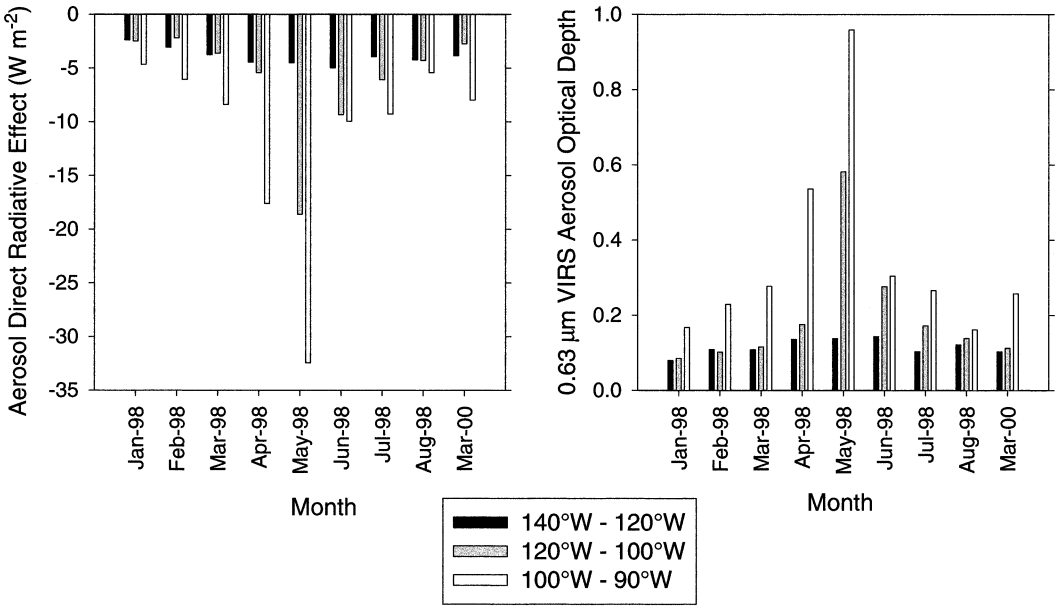

FIG. 6. Spatial and temporal variation of (a) the direct radiative effect and (b) VIRS 0.63-μm aerosol optical depth for biomass burning aerosols near Mexico for latitudes between 15° and 25°N and the indicated longitudes.

($\Delta\alpha/\Delta\tau$) over the Kaashidoo Climate Observatory (KCO) between January–April and May–August 1998. The January–April period over KCO is associated with highly polluted air from the Indian subcontinent (Satheesh and Ramanathan 2000), whereas cleaner conditions prevail during the May–August period due to increased precipitation and a shift in wind direction from northeasterly to southerly. Figure 5a shows smaller $\Delta\alpha/\Delta\tau$ during the polluted January–April period compared to the cleaner May–August period. This is consistent with what is expected theoretically: smaller $\Delta\alpha/\Delta\tau$ is associated with larger particles and/or increased particle absorption; larger $\Delta\alpha/\Delta\tau$ occurs when particles are small and/or less absorbing. As expected, the no aerosol condition—represented by the intercept in Fig. 5b—shows little or no difference for these two time periods. East of the Indian subcontinent (for 0°–20°N, 60°–80°E), the daily average flux per unit VIRS 0.63-μm aerosol optical depth for these two periods is -26.8 W m^{-2} τ^{-1} for January–April (consistent with Satheesh and Ramanathan 2000), and -29.4 W m^{-2} τ^{-1} for May–August 1998.

To examine the influence of biomass burning aerosols on TOA radiation during a dramatic fire event, we consider the 1998 Central American fires that occurred during a period of prolonged drought over Central America and southern Mexico (Peppler et al. 2000). Figure 6 shows the spatial and temporal variation of the aerosol direct radiative effect and the corresponding VIRS 0.63-μm aerosol optical depth for three longitude intervals off of the coast of Mexico. The region farthest from the source of the biomass burning, between 140° and 120°W, has a minimum direct radiative effect of -2.4 W m^{-2} (aerosol optical depth of 0.08) in January, and a maximum in June of -5 W m^{-2} (aerosol optical depth of 0.14). Between 120° and 100°W, the radiative effect ranges from -2.5 W m^{-2} (aerosol optical depth of 0.09) in January to -18 W m^{-2} (aerosol optical depth of 0.58) in May. Closest to the source region, between 100° and 90°W, a minimum of -4.7 W m^{-2} (aerosol optical depth of 0.17) occurs in January—likely due to urban pollution in Mexico City—to a maximum of -32.5 W m^{-2} (aerosol optical depth 0.96) in May due to biomass burning. These results are consistent with Christopher et al. (2000) who found instantaneous SW forcing over the same region and period of ≈ -68 W m^{-2}, which corresponds roughly to a daily mean of -34 W m^{-2}.

When the direct radiative effect of aerosols is stratified by wind speed, a small yet systematic trend is observed. Figure 7 shows the direct radiative effect against wind speed for regions with mean VIRS 0.63-μm aerosol optical depths <0.25 for 15°–25°N and 90°–180°W. As shown, the direct radiative effect becomes more pronounced over this region as wind speeds become stronger. This trend may be physical, as one might expect more sea-salt aerosol generation with increasing wind speed (Blanchard and Woodcock 1980; Hoppel et al. 1990; Flamant et al. 1998), or it could be due to increased transport of aerosols from source regions. Alternately, this trend may instead be an artifact of the retrieval. For example, at large wind speeds, whitecap coverage may increase the observed reflectance from the surface, which can be misinterpreted as an increase in the aerosol direct effect. Haywood et al. (1999) found a similar trend in their comparison of the direct radiative effect of aerosols based on ERBE measurements. In that case, regions where the direct radiative effect was a maximum coincided with regions where the wind speed

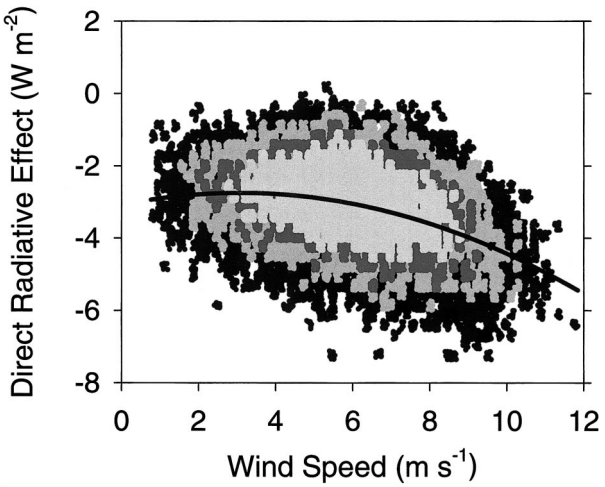

FIG. 7. Aerosol direct radiative effect against wind speed for 1° regions with mean VIRS 0.63-μm aerosol optical depths <0.25 for 15°–25°N and 90°–180°W. Solid line is a second-order polynomial fit through all data points.

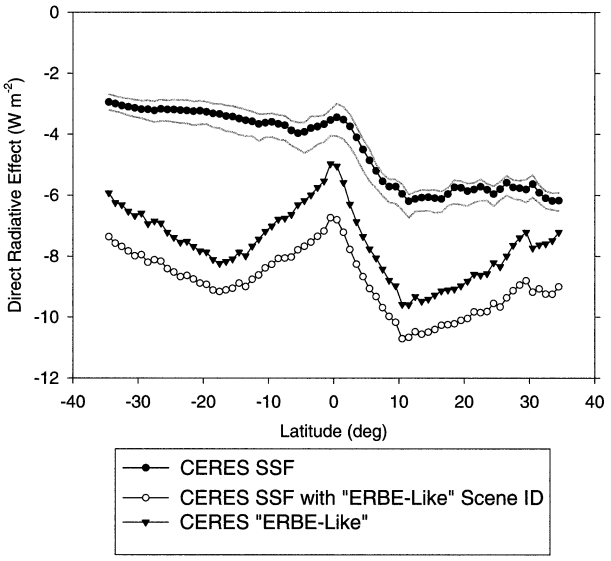

FIG. 8. Sensitivity of aerosol direct radiative effect to clear-sky scene identification. The CERES SSF result corresponds to CERES footprints with all VIRS pixels passing the reflectance, brightness temperature, and infrared/near-infrared difference tests, and more than 50% passing the spatial homogeneity and 3.78-μm channel reflectance tests. Adjacent lines correspond to the case where the percentage of VIRS pixels passing the spatial homogeneity and 3.78-μm channel reflectance tests is 0% or more (lower gray line) and 100% (upper gray line). Open circles show the direct effect using SSF fluxes with scene identification from the CERES/TRMM ERBE-like product. Solid triangles show the direct effect when both TOA fluxes and scene identification are from the ERBE-like product.

was a maximum. To unscramble the various factors that may explain this relationship, it may prove useful to examine statistics of remote marine aerosol optical depth with wind speed from the surface. In that case, the whitecap effect should be eliminated, but other factors, such as wind blown dust at the site and other meteorological influences, may obscure the results.

5. Uncertainties

One of the largest uncertainties in estimating the direct radiative effect of aerosols from satellite measurements is cloud contamination. As noted in section 3c, the cloud mask involves several threshold tests to identify cloud-free CERES footprints. In the present study, footprints are assumed to be cloud free if all VIRS pixels within a CERES footprint pass the reflectance, brightness temperature, and infrared/near-infrared difference tests, and more than 50% pass the spatial homogeneity and 3.78-μm channel reflectance tests. The direct effect was also determined using thresholds of 0% and 100% for the percentage of VIRS pixels within a CERES footprint that pass the spatial homogeneity and 3.78-μm channel reflectance tests. The 0% threshold includes all footprints that pass the reflectance, brightness temperature, and infrared/near-infrared difference tests, while the 100% threshold requires all pixels within a footprint to also pass the spatial homogeneity and 3.78-μm channel reflectance tests. Figure 8 compares the latitudinal dependence in the direct effect for a 50% threshold (solid circles) with results based on thresholds of 0% (bottom gray line) and 100% (top gray line). On average, the difference between the two extreme cases (i.e., 0% and 100%) is $\approx$0.8 W m^{-2}. The direct effect based on the 50% threshold is closer to the 100% threshold result ($\approx$0.29 W m^{-2}) than it is to the 0% threshold values ($\approx$0.46 W m^{-2}). Unfortunately, it remains unclear how this error would change with higher-resolution imager measurements [e.g., 0.25-km Moderate Resolution Imaging Spectroradiometer (MODIS) measurements]. The higher-resolution data would likely significantly improve detection of small-scale and thin clouds, which would tend to reduce the magnitude of the direct effect. However, there may also be conditions in which the current cloud mask is too restrictive and misidentify thicker aerosol layers for cloud. Clearly, more study is needed using instruments that are more sensitive to the presence of cloud [e.g., MODIS, Cloud-Aerosol Lidar and Infrared Pathfinder Satellite Observations (CALIPSO)].

For comparison, Fig. 8 also shows how the direct effect changes when the imager scene identification is replaced by scene identification from the CERES/TRMM ERBE-like product (open circles), and when both the ERBE-like ADMs and scene identification are used to determine the direct effect (solid triangles). The ERBE-like product uses the maximum likelihood estimation technique (MLE; Wielicki and Green 1989) applied to CERES broadband radiances in order to classify a footprint as either clear, partly cloudy, mostly cloudy, or overcast. ERBE ADMs were derived from *Nimbus-7* Earth Radiation Budget (ERB) measurements (Suttles et al. 1988).

When ERBE-like clear-ocean scene identification is used in conjunction with ADMs constructed from the SSF (open circles), the average direct effect reaches ≈ -9 W m^{-2}, a change of ≈ -4.4 W m^{-2} (or a factor of 2) over what is obtained when the imager is used for scene identification. When ERBE-like ADMs are used with MLE scene identification (solid triangles), the average direct effect reaches -7.5 W m^{-2}, or ≈ -3 W m^{-2} more than the SSF value. Clearly, this extra ''forcing'' is caused by cloud contamination. For ERBE, the cloud contamination problem is even more pronounced because the ERBE scanner footprint is at least 4 times larger than a CERES/TRMM footprint. Loeb et al. (2001) showed that an increase in footprint size by a factor of 4 causes a 6% increase in clear-sky ocean radiance using the MLE technique. This occurs because there is a greater likelihood of encountering undetected subresolution clouds when the footprint size is large. Assuming a daily average clear ocean SW flux of 40 W m^{-2}, a 6% increase in SW flux due to cloud contamination would increase the ERBS SW flux by 2.4 W m^{-2} above the CERES ERBE-like SW flux. This means the direct effect for ERBE/ERBS would reach -10 W m^{-2}, or ≈ -5.4 W m^{-2} above the SSF value.

A second source of uncertainty involves the radiance-to-flux conversion [Eq. (3)]. If the ADM is in error, this will introduce a bias in the direct radiative effect estimate. Unfortunately, the ''true'' flux from a scene is usually unavailable. Under limited conditions, one could use highly accurate flux measurements from SW pyranometers aboard aircraft (Hignett et al. 1999) to compare with satellite-based fluxes (provided spatial and temporal matching errors are small). Another approach is to test the consistency in clear-sky instantaneous flux estimates using multiangle measurements of fixed clear-sky targets. Since near-simultaneous fluxes estimated from several different directions over a scene should be the same, multiangle data provide a powerful tool for validating the radiance-to-flux conversion. While the multiangle approach says nothing about the ''absolute'' accuracy of the fluxes themselves, it does provide a good indication of how robust the radiance-to-flux estimate is in different viewing geometries. To perform this test, CERES measurements from nine days when CERES was scanning in the along-track direction are considered. First, SW fluxes from multiangle CERES measurements located over 30-km targets along the ground track are collected. Typically more than 20 multiangle CERES measurements are available over a target region. The imager sees a region from the nadir direction a few minutes prior/after CERES sees the target from an oblique viewing zenith angle. Next, instantaneous fluxes from all viewing directions over the 30-km target regions are converted to albedos. A dispersion parameter (D), determined from the ratio of the albedo standard deviation to the average albedo, is obtained for each 30-km target region. If each footprint within the target region observes the same scene, a perfect ADM would produce a D of zero since albedo should be independent of satellite viewing angle. Figure 9 shows relative frequency distributions of D based on fluxes estimated using the ADMs described in section 3, clear-ocean fluxes from the CERES ERBE-like product, and fluxes based on imager scene identification, but assuming the targets are Lambertian (i.e., no anisotropic correction). As shown, D values are much lower using the ADMs described in section 3 than they are based on ERBE-like and Lambertian fluxes. Average D values ($\overline{D}$) are typically $\approx$2.2% using the ADMs from this study, compared to $\approx$8.8% for the ERBE-like product, and 16.9% when a Lambertian assumption is used. The ERBE-like result is likely influenced both by ADM errors and cloud contamination. To remove the influence of cloud contamination, a fourth case is considered in which only ERBE-like fluxes over targets identified as clear by the imager are used in determining D. In that case, $\overline{D}$ decreases to 5.2%, which is still a factor of 2 larger than results based on the ADMs described in section 3.

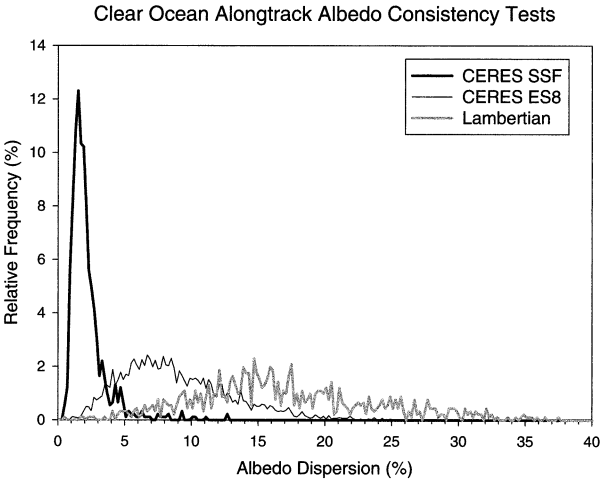

FIG. 9. Relative frequency distributions of multiangle dispersion parameter (D) for albedos estimated using the ADMs described in section 3, clear ocean albedos from the CERES ERBE-like product, and albedos determined assuming the targets are Lambertian (i.e., no anisotropic correction).

To estimate the uncertainty in the mean direct effect due to ADM errors, flux estimates from all nine months of CERES/TRMM observations are sorted by viewing geometry, averaged, and compared with mean fluxes determined by direct integration of the clear-ocean radiances. A similar approach was used in Loeb et al. (1999) and Loeb et al. (2000) to estimate flux uncertainties in all-sky conditions. For clear-ocean scenes, the Helmholtz principle of directional reciprocity is used for filling in angular bins with missing data. Davies (1994) and DiGiroloamo and Davies (1998) showed that while this assumption is questionable under cloudy conditions, it is reasonable for homogeneous scenes, such as clear ocean. Figure 10 shows the ADM and direct integration mean flux difference as a function of solar

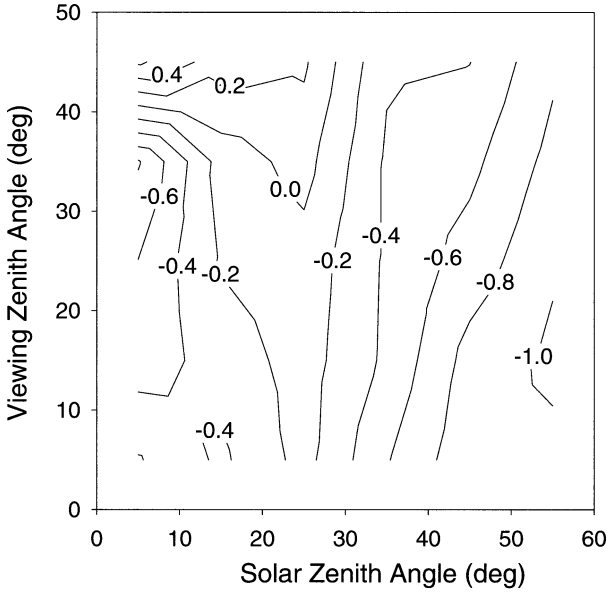

FIG. 10. Difference between mean fluxes estimated from ADMs and fluxes determined by direct integration of mean radiances as a function of solar zenith angle and viewing zenith angle.

zenith angle and viewing zenith angle (averaged over all relative azimuth angle bins). From these results, ADM fluxes are typically lower than direct integration fluxes by 0.4 W m^{-2} (0.5%). This corresponds to a daily average error of ≈0.2 W m^{-2}.

Other factors influencing the uncertainty in the direct effect are instrument calibration and the conversion of filtered SW radiance to unfiltered SW radiance. For CERES/TRMM, the absolute uncertainty in the SW radiances is ≈1% (Priestley et al. 2000), which corresponds to a 0.4 W m^{-2} uncertainty in clear-sky TOA flux, assuming a daily average clear-sky flux of 40 W m^{-2}. The uncertainty in the conversion of filtered SW radiance to unfiltered SW radiance is ≈1% (Loeb et al. 2001). Assuming the error due to cloud contamination is 0.8 W m^{-2} (corresponding to the difference in flux between the upper and lower gray lines in Fig. 8 that bound the CERES SSF aerosol direct radiative effect estimate), and combining errors from cloud contamination, radiance-to-flux conversion, radiance unfiltering, and calibration, the overall error becomes $(0.8^2 + 0.2^2 + 0.4^2 + 0.4^2)^{1/2}$ W m^{-2} or ≈1 W m^{-2} (≈20%). Because of increased cloud contamination associated with the MLE technique, the uncertainty in the CERES ERBE-like direct effect is approximately 3 W m^{-2}. As noted earlier, the cloud contamination problem for ERBE/ERBS is even worse due to its larger footprint. In that case, the error in the direct effect reaches 5.5 W m^{-2}.

6. Summary

This study demonstrates how broadband fluxes from CERES combined with high-resolution imager measurements can be used to estimate the direct radiative effect of aerosols over ocean. Based on nine months of CERES/TRMM measurements, the average direct effect over the tropical oceans is estimated to be −4.6 W m^{-2}. Over the southern tropical oceans, the magnitude of the direct effect is ≈2 W m^{-2} smaller than over the northern tropical oceans. Boucher and Tanré (2000) obtained a similar difference globally (1–3 W m^{-2}) between the Northern and Southern Hemispheres, but the absolute magnitude of their estimates for the global and hemispheric mean direct effect is approximately 1 W m^{-2} larger than that from the present study for the tropical oceans. The CERES-based direct effect is also found to be highly correlated with aerosol optical depth retrievals inferred from 0.63-μm VIRS radiances (correlation coefficient of 0.96) with a slope of ≈−32 W m^{-2} τ^{-1} over the equatorial Pacific Ocean. The slope changes both regionally and seasonally depending on the aerosol characteristics, whereas the intercept remains close to zero, as expected. Temporal and regional changes in the direct effect near sources of biomass burning reach −25 to −30 W m^{-2}, consistent with Christopher et al. (1996). An unexplained result from the present study is the cause for the increase in the direct effect on wind speed. While one might conclude that the increase is related to wind-induced sea-salt aerosols, another contributing factor may be increased surface reflection (e.g., due to whitecaps). A third possibility may simply be due to increased transport of aerosol from source regions with wind speed. The uncertainty in the direct effect is estimated to be 1 W m^{-2}, corresponding to a relative uncertainty of 20%. This error is a factor of 3–5 times smaller than errors associated with estimates based on the ERBE and CERES ERBE-like products.

While the measurements considered in this study cannot be used to provide accurate estimates of the anthropogenic component of the aerosol direct effect over the Tropics, the combination of CERES/Aqua,[1] MODIS/Aqua, and CALIPSO measurements will significantly improve our ability to do so. With these measurements, the anthropogenic aerosol direct effect can be estimated from CERES fluxes over regions identified as having a significant anthropogenic component according to transport model back trajectory analyses initialized using vertical layer information from CALIPSO measurements, and particle size and optical depth information from MODIS. Furthermore, the higher spatial resolution of MODIS data combined with CALIPSO's improved ability to distinguish cloud from aerosol layers will reduce errors due to cloud contamination.

Acknowledgments. The authors would like to thank Dr. James M. Haywood and Professor James A. Coakley Jr. for their helpful comments. This research was funded by the Global Aerosol Climatology Programme (GACP)

[1] The *Aqua* spacecraft, with CERES and MODIS instruments aboard, was successfully launched on 4 May 2002.

under NASA Grant NAG1-2206 and the Clouds and the Earth's Radiant Energy System (CERES) project under NASA Grant NAG-1-2318.

REFERENCES

Ackerman, A. S., O. B. Toon, D. E. Stevens, A. J. Heymsfield, V. Ramanathan, and E. J. Welton, 2000: Reduction of tropical cloudiness by soot. *Science,* **288,** 1042–1047.

Albrecht, B. A., 1989: Aerosols, cloud microphysics, and fractional cloudiness. *Science,* **245,** 1227–1230.

Barkstrom, B. R., 1984: The Earth Radiation Budget Experiment (ERBE). *Bull. Amer. Meteor. Soc.,* **65,** 1170–1186.

Bergstrom, R. W., and P. B. Russell, 1999: Estimation of aerosol direct radiative effects over the midlatitude North Atlantic from satellite and in situ measurements. *Geophys. Res. Lett.,* **26,** 1731–1734.

Blanchard, D. C., and A. H. Woodcock, 1980: The production, concentration, and vertical distribution of the sea-salt aerosol. *Ann. N.Y. Acad. Sci.,* **338,** 330–347.

Boucher, O., and D. Tanré, 2000: Estimation of the aerosol perturbation to the Earth's radiative budget over oceans using POLDER satellite aerosol retrievals. *Geophys. Res. Lett.*, **27,** 1103–1106.

Christopher, S. A., D. V. Vulcan, J. Chou, and R. M. Welch, 1996: First estimates of the radiative forcing of aerosols from biomass burning from satellite data. *J. Geophys. Res.,* **101,** 21 256–21 273.

——, J. Chou, J. Zhang, X. Li, and R. M. Welch, 2000: Shortwave direct radiative forcing of biomass burning aerosols estimated from VIRS and CERES. *Geophys. Res. Lett.*, **27,** 2197–2200.

Coakley, J. A., Jr., R. L. Bernstein, and P. A. Durkee, 1987: Effect of ship-stack effluents on cloud reflectivity. *Science,* **237,** 1020–1022.

Cox, C., and W. Munk, 1955: Some problems in optical oceanography. *J. Mar. Res.,* **14,** 63–78.

Davies, R., 1994: Spatial autocorrelation of radiation measured by the Earth Radiation Budget Experiment: Scene inhomogeneity and reciprocity violation. *J. Geophys. Res.,* **99,** 20 879–20 887.

DiGirolamo, L., T. Varnai, and R. Davies, 1998: Apparent breakdown of reciprocity in reflected solar radiances. *J. Geophys. Res.,* **103,** 8795–8803.

Flamant, C., V. Trouillet, P. Chazette, and J. Pelon, 1998: Wind speed dependence of atmospheric boundary layer optical properties and ocean surface reflectance as observed by airborne backscatter lidar. *J. Geophys. Res.,* **103,** 25 137–25 158.

Haywood, J. M., and O. Boucher, 2000: Estimates of the direct and indirect radiative forcing due to tropospheric aerosols: A review. *Rev. Geophys.,* **38,** 513–543.

——, V. Ramaswamy, and B. J. Soden, 1999: Tropospheric aerosol climate forcing in clear-sky satellite observations over the oceans. *Science,* **283,** 1299–1303.

Hess, M., P. Koepke, and I. Schult, 1998: Optical properties of aerosols and clouds: The software package OPAC. *Bull. Amer. Meteor. Soc.,* **79,** 831–844.

Hignett, P., J. T. Taylor, P. N. Francis, and M. D. Glew, 1999: Comparison of observed and modeled direct aerosol forcing during TARFOX. *J. Geophys. Res.,* **104,** 2279–2287.

Holben, B., and Coauthors, 2001: An emerging ground based aerosol climatology: Aerosol optical depth from Aeronet. *J. Geophys. Res.,* **106,** 12 067–12 097.

Hoppel, W. A., J. W. Fitzgerald, G. M. Frick, R. E. Larson, and E. J. Mack, 1990: Aerosol size and optical properties found in the marine boundary layer over the Atlantic Ocean. *J. Geophys. Res.,* **95,** 3659–3686.

Kato, S., T. P. Ackerman, J. H. Mather, and E. E. Clothiaux, 1999: The *k*-distribution method and correlated-*k* approximation for a shortwave radiative transfer model. *J. Quant. Spectrosc. Radiat. Transfer,* **62,** 109–121.

Kaufman, Y. J., and R. S. Fraser, 1997: The effect of smoke particles on clouds and climate forcing. *Science,* **277,** 1636–1639.

Kiehl, J. T., T. L. Schneider, P. J. Rasch, M. C. Barth, and J. Wong, 2000: Radiative forcing due to sulfate aerosols from simulations with the National Center for Atmospheric Research Community Climate Model, Version 3. *J. Geophys. Res.,* **105,** 1441–1457.

King, M. D., Y. J. Kaufman, D. Tanré, and T. Nakajima, 1999: Remote sensing of tropospheric aerosols from space: Past, present, and future. *Bull. Amer. Meteor. Soc.,* **80,** 2229–2259.

Koepke, P., 1984: Effective reflectance of oceanic whitecaps. *Appl. Opt.,* **23,** 1816–1822.

Li, X., S. A. Christopher, J. Chou, and R. M. Welch, 2000: Estimation of shortwave direct radiative forcing of biomass burning aerosols using angular dependence models. *J. Appl. Meteor.,* **39,** 2278–2291.

Loeb, N. G., P. O'R. Hinton, and R. N. Green, 1999: Top-of-atmosphere albedo estimation from angular distribution models: A comparison between two approaches. *J. Geophys. Res.,* **104,** 31 255–31 260.

——, F. Parol, J.-C. Buriez, and C. Vanbauce, 2000: Top-of-atmosphere albedo estimation from angular distribution models using scene identification from satellite cloud property retrievals. *J. Climate,* **13,** 1269–1285.

——, K. J. Priestley, D. P. Kratz, E. B. Geier, R. N. Green, B. A. Wielicki, P. O'R. Hinton, and S. K. Nolan, 2001: Determination of unfiltered radiances from the Clouds and the Earth's Radiant Energy System (CERES) instrument. *J. Appl. Meteor.,* **40,** 822–835.

Minnis, P., E. F. Harrison, L. L. Stowe, G. G. Gibson, F. M. Denn, D. R. Doelling, and W. L. Smith Jr., 1993: Radiative climate forcing by the Mount Pinatubo eruption. *Science,* **259,** 1411–1415.

——, D. F. Young, B. A. Wielicki, P. W. Heck, X. Dong, L. L. Stowe, and R. Welch, 1999; CERES cloud properties derived from multispectral VIRS data. *Proc. EOS/SPIE Symp. on Remote Sensing,* Florence, Italy, SPIE Proc. 3687, 91–102.

Mishchenko, M. I., I. V. Geogdzhayev, B. Cairns, W. B. Rossow, and A. A. Lacis, 1999: Aerosol retrievals over the ocean by use of channels 1 and 2 AVHRR data: Sensitivity analysis and preliminary results. *Appl. Opt.,* **38,** 7325–7341.

Morel, A., 1988: In-water and remote measurements of ocean color. *Bound.-Layer Meteor.,* **18,** 177–201.

Peppler, R. A., and Coauthors, 2000: ARM Southern Great Plains site observations of the smoke pall associated with the 1998 Central American fires. *Bull. Amer. Meteor. Soc.,* **81,** 2563–2591.

Priestley, K. J., and Coauthors, 2000: Post launch radiometric validation of the Clouds and the Earth's Radiant Energy System (CERES) proto-flight model on the Tropical Rainfall Measuring Mission (TRMM) spacecraft through 1999. *J. Appl. Meteor.,* **39,** 2249–2258.

Rabier, F., J.-N. Thepaut, and P. Courtier, 1998: Extended assimilation and forecast experiments with a four-dimensional variational assimilation. *Quart. J. Roy. Meteor. Soc.,* **124,** 1861–1887.

Satheesh, S. K., and V. Ramanathan, 2000: Large differences in tropical aerosol forcing at the top the atmosphere and Earth's surface. *Nature,* **405,** 60–63.

——, ——, X. Li-Jones, J. M. Lobert, I. A. Podgorny, J. M. Prospero, B. N. Holben, and N. G. Loeb, 1999: A model for the natural and anthropogenic aerosols over the tropical Indian Ocean derived from INDOEX data. *J. Geophys. Res.,* **104,** 27 421–27 440.

Stamnes, K., S. C. Tsay, W. Wiscombe, and I. Laszlo, 2000: A general-purpose numerically stable computer code for discrete-ordinate-method radiative transfer in scattering and emitting layered media. DISORT Rep. v1.1, 112 pp. [Available online at ftp://climate.gsfc.nasa.gov/pub/wiscombe/Multiple_Scatt/DISTORTReport1.1.pdf.]

Stowe, L. L., A. M. Ignatov, and R. R. Singh, 1997: Development, validation and potential enhancements to the second generation

operational aerosol product at NOAA/NESDIS. *J. Geophys. Res.*, **102,** 16 923–16 934.

——, P. A. Davis, and E. P. McClain, 1999: Scientific basis and initial evaluation of the CLAVR-1 global clear/cloud classification algorithm for the Advanced Very High Resolution Radiometer. *J. Atmos. Oceanic Technol.*, **16,** 656–681.

Suttles, J. T., and Coauthors, 1988: Angular radiation models for Earth–atmosphere systems. Vol. I. Shortwave models. NASA Rep. RP-1184, Washington, DC, 144 pp.

Trepte, Q., Y. Chen, S. Sun-Mack, P. Minnis, D. F. Young, B. A. Baum, and P. W. Heck, 1999: Scene identification for the CERES cloud analysis subsystem. Preprints, *10th Conf. on Atmospheric Radiation*, Madison, WI, Amer. Meteor. Soc., 169–172.

Twomey, S., 1974: Pollution and the planetary albedo. *Atmos. Environ.*, **8,** 1251–1256.

Vermote, E., D. Tanré, J. L. Deuzé, M. Herman, and J. J. Morcette, 1997: Second simulation of the satellite signal in the solar spectrum: An overview. *IEEE Trans. Geosci. Remote Sens.*, **35,** 675–686.

Wielicki, B. A., and R. N. Green, 1989: Cloud identification for ERBE radiation flux retrieval. *J. Appl. Meteor.*, **28,** 1133–1146.

——, B. R. Barkstrom, E. F. Harrison, R. B. Lee III, G. L. Smith, and J. E. Cooper, 1996: Clouds and the Earth's Radiant Energy System (CERES): An earth observing system experiment. *Bull. Amer. Meteor. Soc.*, **77,** 853–868.

Young, D. F., P. Minnis, D. R. Doelling, G. G. Gibson, and T. Wong, 1998: Temporal interpolation methods for the Clouds and the Earth's Radiant Energy System (CERES) Experiment. *J. Appl. Meteor.*, **37,** 572–590.